

## Research



**Cite this article:** Ledesma-Alonso R, Raphaël E, Léger L, Restagno F, Poulard C. 2016 Stress concentration in periodically rough Hertzian contact: Hertz to soft-flat-punch transition. *Proc. R. Soc. A* **472**: 20160235. <http://dx.doi.org/10.1098/rspa.2016.0235>

Received: 31 March 2016

Accepted: 19 August 2016

### Subject Areas:

mechanical engineering, computational mechanics, mechanics

### Keywords:

patterned substrate, surface fraction, stress concentration, real contact area, Hertz to soft-flat-punch transition

### Author for correspondence:

R. Ledesma-Alonso

e-mail: [rene.ledesma-alonso@epsci.fr](mailto:rene.ledesma-alonso@epsci.fr)

Electronic supplementary material is available at <http://dx.doi.org/10.1098/rspa.2016.0235> or via <http://rspa.royalsocietypublishing.org>.

# Stress concentration in periodically rough Hertzian contact: Hertz to soft-flat-punch transition

R. Ledesma-Alonso<sup>1,2</sup>, E. Raphaël<sup>1</sup>, L. Léger<sup>2</sup>,  
F. Restagno<sup>2</sup> and C. Poulard<sup>2</sup>

<sup>1</sup>Laboratoire de Physico-Chimie Théorique, UMR CNRS 7083 Gulliver, ESPCI ParisTech, PSL Research University, 10 Rue Vauquelin, 75005 Paris, France

<sup>2</sup>Laboratoire de Physique des Solides, CNRS, Université Paris-Sud, Université Paris-Saclay, 91400 Orsay, France

RL-A, 0000-0001-5690-5034

We report on the elastic contact between a spherical lens and a patterned substrate, composed of a hexagonal lattice of cylindrical pillars. The stress field and the size of the contact area are obtained by means of numerical methods: a superposition method of discrete pressure elements and an iterative bisection-like method. For small indentations, a transition from a Hertzian to a soft-flat-punch behaviour is observed when the surface fraction of the substrate that is covered by the pillars is increased. In particular, we present a master curve defined by two dimensionless parameters, which allows one to predict the stress at the centre of the contact region in terms of the surface fraction occupied by pillars. The transition between the limiting contact regimes, Hertzian and soft-flat-punch, is well described by a rational function. Additionally, a simple model to describe the Boussinesq–Cerruti-like contact between the lens and a single elastic pillar, which takes into account the pillar geometry and the elastic properties of the two bodies, is presented.

## 1. Introduction

The contact mechanics between an elastic sphere and a flat elastic solid, with frictionless, perfectly smooth and non-conforming surfaces, is beautifully provided by the Hertz theory [1]. From the knowledge of the geometry (sphere radius  $R$ ), the elastic properties (Young's

modulus and Poisson's ratio) and the total load  $F$  compressing the two elastic solids, one can forecast the radius of contact  $a \sim \sqrt[3]{RF}$ , the total indentation  $\zeta \sim \sqrt[3]{F^2/R}$  of the two bodies and the maximum pressure  $\sigma_{0H} \sim \sqrt[3]{F/R^2}$ . When adhesion between the two bodies in contact is considered, several modifications from the Hertz theory have been proposed: (i) the Johnson–Kendall–Roberts (JKR) model, which accounts for the attractive surface forces inside the contact region, predicts a larger contact radius than the Hertzian value and applies for soft materials, (ii) the Derjaguin–Muller–Toporov (DMT) model, which considers that the attractive forces act only outside the contact region, infers a Hertzian contact profile but with larger deformations (compared with the Hertz theory) for the same load, and suits for hard materials. Finally, the Maugis–Dugdale (MD) model describes an unified way in precisely the transition between the two previous models.

However, real surfaces are not smooth and the contact mechanics of two real bodies can bitterly deviate from the Hertzian predictions since only partial contact can occur [1–3]. Attention has been paid to this problem from two different points of departure, the first based on a statistical approach of real surfaces and the second on the deterministic behaviour of periodic surfaces.

On the one hand, the statistical approach to the contact mechanics of real surfaces bifurcates into three branches. First, considering the contact between a plane and an isotropically rough surface composed of non-interacting 'spherical asperities' with a vertical position given by a distribution of heights (exponential and Gaussian) [4–6], from which estimations of the number of contact spots, the contact area and the total load were obtained in terms of the apparent contact area, the density of asperities, the radius of curvature of the asperities and a function of the heights distribution. In particular, it has been found that both the number of asperities in contact and the real contact area are proportional to the total load [4], and the ratio of the roughness to the indentation has been proposed as a parameter to account for the influence of the roughness on the contact mechanics [5,6]. Additionally, useful empirical elasto-plastic models can be found in the recent literature [7,8], which consider nominally rough surfaces and are based on the above-mentioned statistical approaches. Second, a similar approach to the previous one was developed, but considering a distribution for the shapes of the asperities, i.e. an isotropically rough surface composed of non-interacting 'paraboloid-like asperities' with a Gaussian distribution of the slopes and curvatures [9]. It has been shown that considering roughness, given by a bandwidth of wavelengths, the real contact area is strictly proportional to the load and, thus, the stress distribution at the average asperity contact region remains unchanged. Nevertheless, the two above-mentioned approaches break down for large loads, at which the separation between the contact surfaces becomes small and the interaction between adjoining asperities cannot be neglected. Finally, the surface roughness power spectrum, for instance, self-affine fractal surfaces and frozen capillary waves, was employed to estimate the ratio between the real and apparent contact areas [10]. This description is particularly accurate for high loads, and it is based on the knowledge of the stress distribution, which depends on the average pressure and the magnification (the ratio between size of the apparent contact area and the shortest wavelength roughness). It also predicts a linear dependence of the real contact area on the total load, for small loads and small real-to-apparent contact area ratios. Even though the aforementioned statistical methods provide average quantities and global insight of the rough contact phenomenon, the local stress and displacement fields at the contact spots remain inaccessible since the surface topography may not be persistent from one body to another.

On the other hand, in order to gain insight on the local response of the bodies in contact, periodic contact problems have been addressed [11,12]. For instance, the contact between a flat surface and a well-characterized one-dimensional wavy surface, of wavelength  $\lambda$  and amplitude  $\delta$ , has been addressed by superposition of concentrated normal forces at the surface of an infinite half-space (Boussinesq–Cerruti approach). In this situation, a close-form solution for the stress and displacement fields is obtained and we should encourage the interested reader to review the aforementioned bibliography. However, we should mention that for a given line load  $F$ , the local contact occurs in bands of increasing width  $2a$  that obey the scaling  $F \sim \delta \sin^2(\pi a/\lambda)$  with a maximum stress  $\sigma_0 \sim (\delta/\lambda) \sin(\pi a/\lambda)$ . Following the same ideas, a well-characterized

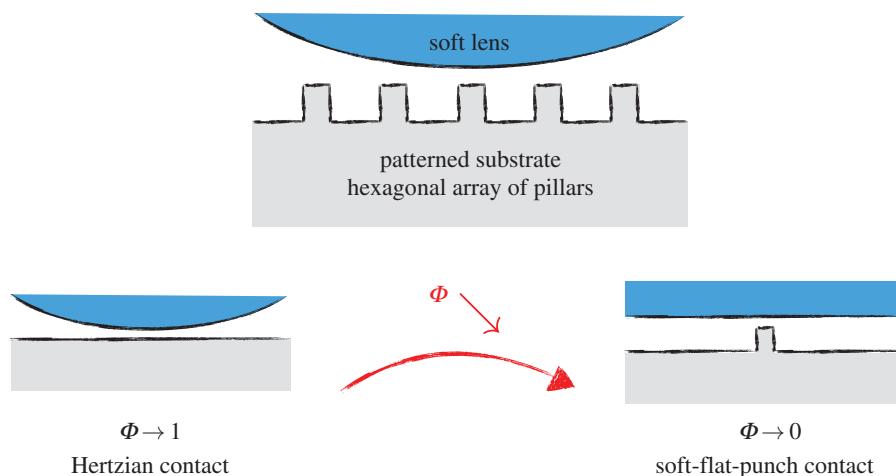


**Figure 1.** Illustration of the discrete contact problem studied in this manuscript and its asymptotic cases, with respect to the surface fraction  $\Phi$  of the substrate that is occupied by the pillars. (Online version in colour.)

two-dimensional regular and orthogonal wavy surface was analysed but only asymptotic behaviours have been discerned. In particular, for light loads, a local Hertzian behaviour is expected at the contact between the plane and each summit of the wavy surface, a nearly circular region of contact of radius  $a \sim \sqrt[3]{F}$  is observed. Despite these efforts, the size of the contact region and the stress field provoked by the contact of rough finite-size surfaces remains not predicted by the discussed deterministic method.

Understanding the contact mechanics of rough surfaces, starting with well-controlled patterned surfaces, is fundamental in order to clarify the effect of pattern covering on friction [13–18], or to identify the influence of texturation on the adhesive properties of surfaces [19–22]. This query has received a lot of attention since patterned surfaces have been extensively used as biomimetic surfaces [23–28]. From this point of view, one of the important issues is the contact formation, which fixes the relationship between the measured adhesion and the preload before the detachment [29,30].

In the simplest case of a spherical lens on well-controlled patterned surface made on elastomeric PDMS with circular bumps and cylindrical pillars, a transition from suspended (the lens touches only the top of the bumps/pillars) to intimate contact (the lens gets in contact not only with the bumps/pillars but also with the underlying substrate in between the patterns) has been observed. The contact formation has been shown to depend strongly on the geometry and elastic properties of the textured surface [3,31–33]. In particular, Verneuil and co-workers [31] have shown that the one leading parameter is the surface fraction  $\Phi$  occupied by the pillars, since the critical force, which marks the threshold between both contact regimes, scales as  $F_c \sim \Phi^3$ .

Therefore, there is no doubt about the central role that the surface fraction  $\Phi$  plays in the distribution of stresses and in ascertaining the size of the contact region. The geometry of a sphere in contact with an array of cylindrical pillars is represented graphically in figure 1. When  $\Phi \rightarrow 1$ , a classic problem consisting in the contact mechanics of a sphere and a half-space is recovered, for which the stress and displacement fields are described by the Hertz theory. At the opposite limit, when  $\Phi \rightarrow 0$  the contact mechanics is no longer a Hertzian contact but should be represented by the compression of a half-space and a cylindrical pillar, as depicted in figure 1. The indentation of an elastic half space by a flat rigid punch is described by the classical Boussinesq–Cerruti solution, which is obtained either by the superposition of concentrated normal forces [1,34] or by means of a Hankel transform method with an imposed surface displacement [35,36]. As well, an analysis, which has remained out of focus, presents a numerical solution that provides the transition from the limit case of the contact between a rigid punch and an elastic half-space to the opposite case

of an elastic cylinder and a rigid flat surface [37]. Nevertheless, the passage from one regime to another is not obvious and work must be done to describe clearly this phenomenon. This is precisely the object of the present article.

In this paper, we discuss the elastic contact between a spherical lens and patterned surface with cylindrical pillars. The presented analysis, which corresponds to a first approach on the real contact mechanics of periodic rough surfaces, considers two fundamental hypotheses: (i) frictionless contact and (ii) no adhesion effects. The impact of elastic properties and of the geometry of the system is analysed, with special focus on the surface fraction occupied by the pillars. A detailed description of the transition from Hertzian contact (short pitch distance) to soft-flat-punch (SFP) regime (large pitch distance), for the aforementioned lens-patterned substrate system, is presented. We will discuss the contact behaviour for a wide range of elastic parameters (combination of Young's modulus) and displacement of the bodies (total indentation), and analyse the effects of the pitch between pillars in terms of the stress concentration and the number of pillars (real contact area) within the contact region.

## 2. System description

Consider an elastic system formed by a semi-infinite substrate, the upper surface of which is patterned with a hexagonal lattice of cylindrical pillars, and a spherical lens. We imagine a situation in which the lens is pushed against the substrate, whereas the latter is fixed at the far-field, with respect to the lens initial position. A discrete mechanical contact region (for small loads) occurs, which produces and conveys stress and displacement fields at the lens and the substrate. In brief, once a load is applied, the system evolves from an initial undeformed state, at which the lowest point of the lens touches in a single point the centre of the top of a central pillar, towards a final deformed state, where multiple contact regions appear. We expect to observe deviations from this general trend, depending on the specific geometry of the system and the magnitude of the applied load.

Herein, we consider another important hypothesis: the effect of lateral displacement, due to the discrete stress field is negligible with respect to normal displacement. Our intuition leads us to imply that the lateral displacement provoked by a single pillar is cancelled by the lateral displacement generated by the surrounding pillars and, as a result, the superposition of the effects of all the pillars can be neglected. In addition, also due to the aforementioned idea, the patterned substrate can be further separated. To be more precise, the system, represented in figure 2, can be decomposed into several independent bodies: (i) a spherical lens, a cap that corresponds to the lower region of a sphere of radius  $R$ ; (ii) a flat substrate, which we will take as an elastic half-space; and (iii) an array of cylinders, where  $d$  and  $h$  are, respectively, the diameter and height of each pillar, whereas  $e$  is the pitch, the distance between the centre of two pillars.

### (a) Array of pillars

When the lens is pushed against the patterned substrate, the number of pillars in contact  $Q$  can be estimated by using the Wigner-Seitz cell of an hexagonal lattice of pillars (figure 2). Computing the fraction of the surface occupied by the pillars:

$$\Phi = \frac{\pi}{2\sqrt{3}} \left(\frac{d}{e}\right)^2, \quad (2.1)$$

and, considering a circular region of radius  $a$  as the apparent contact zone, the number of pillars in contact becomes

$$Q \approx \frac{2\pi}{\sqrt{3}} \left(\frac{a}{e}\right)^2. \quad (2.2)$$

Nevertheless, one cannot predict an accurate number of pillars  $Q$  because the apparent contact radius  $a$  is unknown *a priori*. Despite this fact, in the present study we will consider that  $R \gg d/2$  and  $R \gg a$  which corresponds to a lot of practical situations previously studied in the literature.

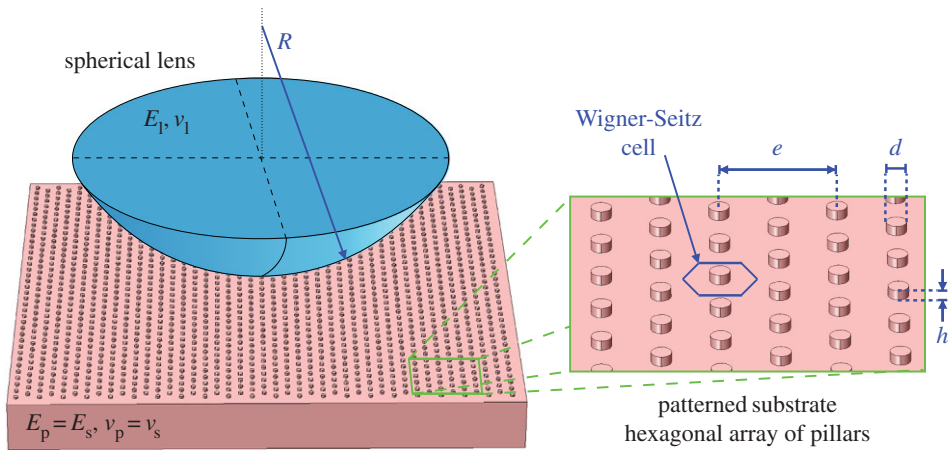


**Figure 2.** Schematic of the lens-substrate system. Both bodies are made of elastic materials: the lens is a spherical cap, whereas the substrate consists of a half-space with an hexagonal array of cylindrical pillars at its upper surface. The elastic properties ( $E$  Young's modulus and  $\nu$  Poisson's ratio) of the components and their relevant dimensions ( $R$  lens radius,  $d$  diameter and  $h$  height of the pillars and  $e$  pitch distance) are shown. The subindices  $l$ ,  $p$  and  $s$  correspond to lens, pillars and substrate, respectively. (Online version in colour.)

Considering a polar system  $(r, \theta)$ , the position of the centre of the  $i$ th pillar is given by the coordinates  $(r_i, \theta_i)$ , where the value of  $i = 0$  corresponds to the pillar whose centre is placed at the origin of the coordinate system. A detailed description of the pillar array and the precise method to enumerate the pillars and to count the number of pillars in contact is given in the electronic supplementary material.

## (b) Displacement and indentation

Before the lens and patterned substrate are squeezed and the deformation of both bodies takes place, the centre of the spherical lens is placed at  $z = h + R$ . In turn, the equation of the pillars-substrate surface is

$$g^\circ(r, \theta) = h \sum_{i=0}^Q \left[ 1 - H \left( \rho_i - \frac{d}{2} \right) \right], \quad (2.3)$$

where  $H$  is a Heaviside step function, taking either the value of 0 if  $\rho_i \leq d/2$  or 1 if  $\rho_i > d/2$ . As described in the electronic supplementary material relative to the centre of the  $i$ th pillar, which is placed at  $(r_i, \theta_i)$ ,  $\rho_i$  is the distance to the point  $(r, \theta)$ , given by

$$\rho_i = \sqrt{r^2 + r_i^2 - 2rr_i \cos(\theta - \theta_i)}. \quad (2.4)$$

These initial positions indicate that the lens and the patterned substrate are in contact at a single point, at  $r = 0$  where the lowest position of the lens touches the centre of the pillar upper surface.

Once the load is applied and the system has attained equilibrium, the final gap between the surfaces, the space separating the lens and the pillar-substrate body, is now given by

$$\Delta(r, \theta) = h + R - \sqrt{R^2 - r^2} - g^\circ(r, \theta) + w(r, \theta) - \zeta, \quad (2.5)$$

where  $w(r, \theta)$  is the total displacement field and  $\zeta = w(0, \theta)$  is the indentation, i.e. the displacement at the centre. For light loads and within the apparent contact region, only the top of the pillars can be in contact with the lens, whereas the substrate not covered by pillars will be separated from the lens by a gap. In addition, one may note that, within the contact region, the top of each pillar may be either in total or partial contact. Whatever the contact situation of each pillar, at the local

contact regions, one has  $\Delta(r, \theta) = 0$  and  $g^\circ(r, \theta) = h$ , and thus the total displacement field  $w(r, \theta)$  is related to the total indentation  $\zeta$  as follows:

$$w(r, \theta) = \zeta - [R - \sqrt{R^2 - r^2}]. \quad (2.6)$$

### 3. Discrete contact

For each body  $j$  (lens  $j = l$ , array of pillars  $j = p$  and substrate  $j = s$ ), considering its Young's elastic modulus  $E_j$  and Poisson's ratio  $\nu_j$ , we define the parameter  $\gamma_j = [1 - \nu_j^2]/E_j$ . Herein, we will always consider that the pillars and the substrate are made of the same material, thus  $E_p = E_s$  and  $\nu_p = \nu_s$ . As mentioned above, when these bodies are brought into contact, i.e. the lens is approached towards the pillars, which in turn pushes the substrate, they suffer a deformation. Under these circumstances, recalling that the vertical displacement at the surface of a half-space  $u_z$  due to a concentrated point force  $\Sigma$  is given by [1]

$$u_z(\Sigma, r) = \frac{\gamma \Sigma}{\pi r}, \quad (3.1)$$

and applying the principle of linear superposition, the normal displacement of the spherical lens and the substrate ( $j = l, s$ ) reads

$$w_j(r, \theta) = \iint_{\mathcal{A}} u_z(\sigma, \varrho) \varrho \, d\varrho \, d\varphi, \quad (3.2)$$

where  $\sigma = \sigma(\varrho, \varphi)$  is the stress field over the apparent contact area  $\mathcal{A}$ , which is described by  $\varrho$  and  $\varphi$ , the radial and angular coordinates relative to the point  $(r, \theta)$ . In other words, the displacement  $w_j$  at the point  $(r, \theta)$  is the effect of the stress field applied over a region described by the set of relative positions  $(\varrho, \varphi)$ . Owing to the discrete nature of the contact, the normal displacement of each surface can be decomposed as follows:

$$w_j(r, \theta) = \frac{\gamma_j}{\pi} \sum_{i=0}^Q W_i(r, \theta, r_i, \theta_i) \quad \text{and} \quad W_i(r, \theta, r_i, \theta_i) = \int_{\varphi_{i1}}^{\varphi_{i2}} \int_{\varrho_{i1}}^{\varrho_{i2}} \sigma(\varrho, \varphi) \, d\varrho \, d\varphi, \quad (3.3)$$

where  $W_i$  is the reduced displacement at  $(r, \theta)$  due to the contact with the  $i$ th pillar. Additionally, we make emphasis on the fact that the displacement field  $W_i$  depends explicitly on the position of the  $i$ th pillar, since the integration limits  $\varrho_{i1}$ ,  $\varrho_{i2}$ ,  $\varphi_{i1}$  and  $\varphi_{i2}$  must be determined for each combination of pillar location  $(r_i, \theta_i)$  and point  $(r, \theta)$ . For instance,  $\varrho_{i1}$  and  $\varrho_{i2}$  are the solutions for  $\varrho$  of quadratic equation

$$\varrho^2 - [2\rho_i \cos(\varphi)]\varrho + \left[ (\rho_i)^2 - \left( \frac{d}{2} \right)^2 \right] = 0, \quad (3.4)$$

where  $\rho_i = \rho_i(r, \theta, r_i, \theta_i)$  given in equation (2.4), whereas  $\varphi_{i1}$  and  $\varphi_{i2}$  depend on the location of the point  $(r, \theta)$ . On the one hand, if  $(r, \theta)$  lies inside the contact region of the  $i$ th pillar, we have  $\varphi_{i1} = 0$  and  $\varphi_{i2} = \pi$ , and, on the other hand, if  $(r, \theta)$  is located outside the contact region of the  $i$ th pillar, we find

$$\varphi_{i1,2} = \pm \arcsin \left( \frac{[d/2] \sin(\pi/2)}{\rho_i} \right). \quad (3.5)$$

In turn, each pillar is compressed because of its confinement between the lens and the substrate. Herein, we consider that the compression of the  $i$ th pillar is approximated by Hooke's Law, which gives a change of height equal to  $\delta_i = 4hF_i/(\pi d^2 E_p)$ . As well,  $F_i$  is the load exerted over the  $i$ th pillar in the contact region, which reads

$$F_i(r_i, \theta_i) = \int_0^{2\pi} \int_0^{d/2} \sigma(\rho_i, \phi_i) \rho_i \, d\rho_i \, d\phi_i, \quad (3.6)$$

whereas, in this situation,  $\rho_i$  and  $\phi_i$  represent, respectively, the radial and angular coordinates at the surface of the  $i$ th pillar, relative to the pillar centre  $(r_i, \theta_i)$  and restricted to the ranges  $\rho_i \in [0, d/2]$  and  $\phi_i \in [0, 2\pi]$ . In order to transform, the stress field over the entire domain  $\sigma(r, \theta)$  into



$\sigma(r_i, \theta_i, \rho_i, \phi_i)$ , one should express  $r$  and  $\theta$  for a given relative position  $(\rho_i, \phi_i)$  and a pillar  $(r_i, \theta_i)$  using the following expressions:

$$r = \sqrt{\rho_i^2 + r_i^2 + 2\rho_i r_i \cos(\phi_i - \theta_i)} \quad \text{and} \quad \theta = \arcsin\left(\frac{\rho_i \sin(\pi - \phi_i) + r_i \sin(\theta_i)}{r}\right). \quad (3.7)$$

Additionally, the total load  $F_T$  reads

$$F_T = \iint_{\mathcal{A}} \sigma(r, \theta) r \, dr \, d\theta, \quad (3.8)$$

which, accounting with the discrete nature of the contact, can be obtained by adding the contribution of each pillar as follows:

$$F_T = \sum_{i=0}^Q F_i(r_i, \theta_i). \quad (3.9)$$

Since, the total displacement field is also composed of

$$w(r, \theta) = w_1(r, \theta) + w_s(r, \theta) + \frac{\delta_i g^\circ(r, \theta)}{h}, \quad (3.10)$$

which gathers the displacement contributions given in equation (3.3) and the Hookean pillar compression  $\delta_i$ , imposing a total indentation, given by equation (2.6) and evaluated at the top of the pillars where  $g^\circ(r, \theta) = h$ , allows one to recover the stress field  $\sigma$  inside the contact region. Herein,  $\sigma$  is computed numerically using a superposition method of discrete pressure elements, for which a segmentation of each contact region (the top of each pillar) into square subregions of constant constraint is performed. Details are given in the electronic supplementary material. A similar approach has been introduced and validated in previous studies [38,39], for which a Hookean hypothesis and a uniform pressure has been applied to each pillar. Even though our methodology retains the Hookean behaviour for each pillar, it allows the appearance of non-axisymmetric pressure fields for the non-centred pillars ( $i > 0$ ), thanks to the discretization of each contact region. This procedure provides a more realistic approach for several cases, including small total loads  $F_T$  and small surface fractions  $\Phi$ , but also the effect of the finite size of the contact area, for any load and any surface fraction. The corresponding results are presented in the following section.

## 4. Results

In figure 3a, the contact region and the stress field for a small surface fraction  $\Phi = 0.03$  is depicted for  $E_p = E_s = 1.6 \times 10^6$  Pa,  $\zeta = 0.3 \mu\text{m}$ , two particular indentations and all other parameter values given in table 1. The contact radius is approximately equal to  $a \approx e + d/2 = 26 \mu\text{m}$ . For the pillar at the centre of the contact region, it turns out that the stress field is equivalent to a soft-flat-punch (SFP) stress field. The stress field is axisymmetric, with a large gradient, i.e. small  $\sigma$  around the central zone  $r \approx 0$  and very large  $\sigma$  near the edge of the pillar  $r \lesssim d/2$ . We clearly observe an increase in an order of magnitude when going from the centre to the border of this pillar. In addition, within the primitive cell, a second pillar is in contact, subjected to a stress field which is only symmetric with respect to the plane  $\theta = 0$ . This field is eccentric with respect to the centre of the pillar, leading to slightly oblate iso-stress contour lines, which recover the centric and circular shape as the border of the pillar is reached. The increase of stress magnitude, from the centre to the border of the pillar, is very similar to the one observed for the central pillar. The stress  $\sigma$  at the central region of both pillars seems to follow a Hertzian-like behaviour, a square root profile calculated with the stress  $\sigma_0$  at  $r = 0$  and the contact radius  $a$  obtained from the simulations. As expected, relatively high magnitudes of the ‘discrete’ stress field are observed in this case, since the total load is concentrated over seven pillars, considering the geometry of the system. For comparison, the Hertzian stress profile is plotted in the figure.

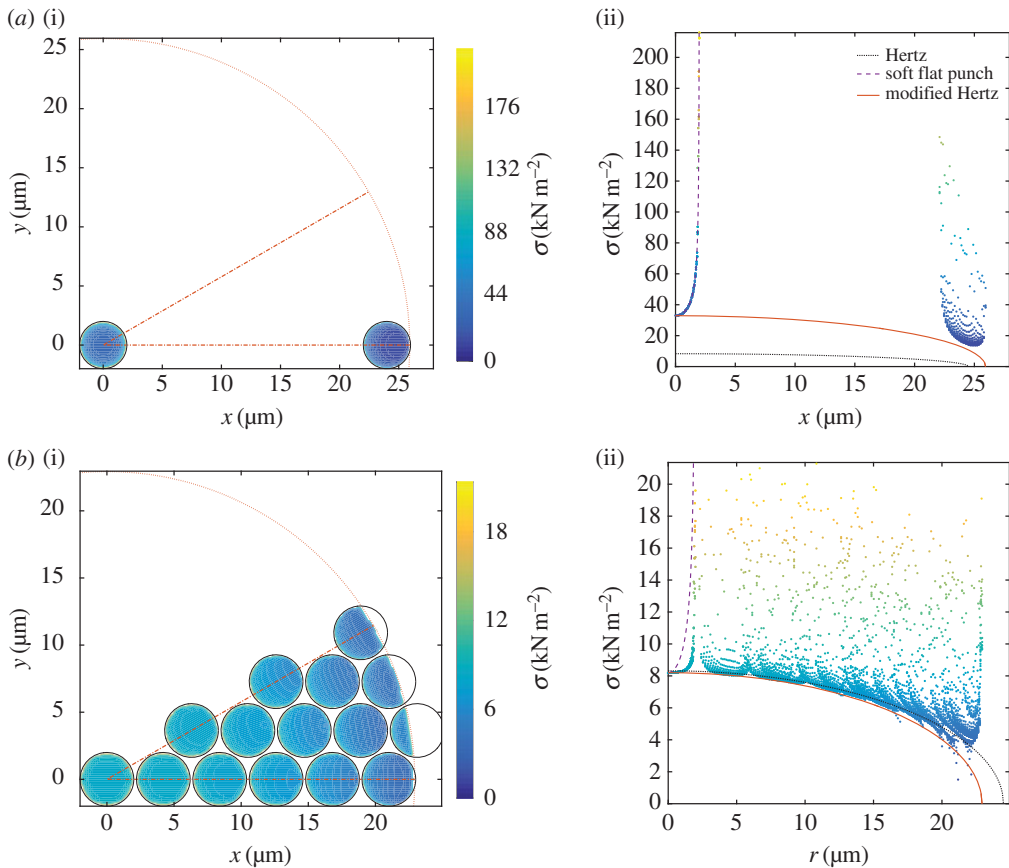


**Figure 3.** Stress field at the contact region  $\sigma$  within the primitive cell of the system delimited by the dashed lines, obtained for  $E_p = E_s = 1.6 \times 10^6$  Pa,  $\zeta = 0.3 \mu\text{m}$ , different values of  $\Phi$ —(a)  $\Phi = 0.03$  and (b)  $\Phi = 0.82$ —and the remaining parameter values given in table 1. The dotted curves delimitate the computed contact region for each case. *a(i)* and *b(i)* show a two-dimensional representation in the plane  $xy$ , whereas *a(ii)* and *b(ii)* show a one-dimensional representation in the axis  $r = \sqrt{x^2 + y^2}$ . In the  $\sigma$  versus  $r$  representation, curves indicating the Hertz and soft-flat-punch stress fields, given, respectively, by equations (5.1) and (5.3), and a modified Hertz-like behaviour, for which the stress  $\sigma_0$  at  $r = 0$  and the apparent contact radius  $a$  were obtained from the numerical simulations, are also depicted. (Online version in colour.)

**Table 1.** The values of the parameters used to obtain the presented results.

parameter	values	units
$R$	2	mm
$h$	2	$\mu\text{m}$
$d$	4	$\mu\text{m}$
$\Phi$	$[2.3 \times 10^{-3}, 8.2 \times 10^{-1}]$	1
$\zeta$	$[0.005, 0.5]$	$\mu\text{m}$
$E_l$	$1.6 \times 10^6$	Pa
$E_p = E_s$	$[10^3, 10^{12}]$	Pa
$\nu_l$	0.5	1
$\nu_p = \nu_s$	0.5	1



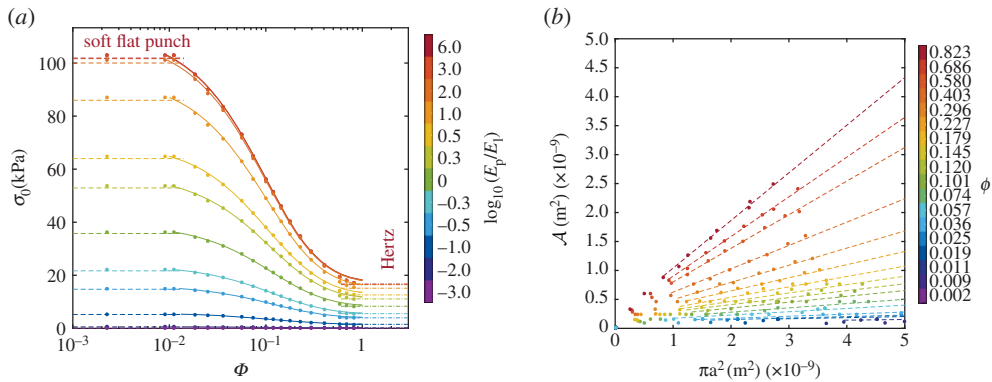


**Figure 4.** (a) Stress at the centre of the contact region  $\sigma_0$ , for  $\zeta = 0.3 \mu\text{m}$  and the remaining parameters given in table 1. Different pillar-substrate stiffnesses, from (top/red) hard to (bottom/violet) soft materials, are presented. Continuous lines were obtained from equation (6.4) and the corresponding fit of  $\Phi_H \in [0.306, 0.38]$  and  $\Phi_S \in [0.0094, 0.0135]$ —both from hard to soft materials, for each set of parameters. The Hertzian and soft-flat-punch values were computed with equations (5.2) and (5.7), respectively. (b) Real contact area  $A$  as functions of the apparent contact area  $\pi a^2$ , for  $E_p/E_l = 1$  and the remaining parameters given in table 1. Dashed lines (from (top/red) high to (bottom/violet) low surface fraction  $\Phi$ ) indicate the linear dependence  $A = \Phi[\pi a^2]$ , expected to be the asymptotic behaviour for relatively large indentations  $\zeta$  and, thus, large apparent contact radius  $a$ . (Online version in colour.)

For the same indentation and Young's modulus, the contact region and the stress field for a large surface fraction  $\Phi = 0.82$  is illustrated in figure 3b. The contact radius is approximately equal to  $a \approx 5e + d/2 = 23 \mu\text{m}$ , slightly smaller than the radius of the small  $\Phi = 0.03$  case. The behaviour of  $\sigma$  at the central pillar deviates strongly from the SFP profile, with a nearly constant stress magnitude at the centre region  $0 \leq r \leq d/4$ , that diverges rapidly as the border is reached (a stress profile similar to the ones found by Gecit [37]). Nevertheless, the stress profile remains axisymmetric and its magnitude is relatively small over the entire lid of the pillar. For the other pillars, which are not at  $r = 0$ , the local stress field is only symmetric with respect to the corresponding plane  $\theta = \theta_i$  of the  $i$ th pillar. Oblate iso-stress contour zones, nearly crescent-like shapes, are found, mainly for the pillars near the border of the contact region. Once more, considering  $\sigma$  at the central region of each pillar, a Hertzian stress field is observed, with the usual square root profile computed with a stress  $\sigma_0$  at  $r = 0$ , very close to the true Hertz value, and a contact radius  $a$  that is significantly smaller than the true Hertz contact radius.

It is important to note that, while a constant indentation  $\zeta$  is kept for the cases presented in figure 3, a reduction of  $\sigma_0$ , of one order of magnitude (from 33 to 8 kPa) when  $\Phi$  is increased (from 0.03 to 0.82), is observed. As well, the same increase of  $\Phi$  produces a reduction of the apparent contact region and the contact radius  $a$  (from 26 to 23  $\mu\text{m}$ ), but the real contact area given by the number of pillars in contact has increased, even though the total load  $F_T$  has risen (from 3 to 10  $\mu\text{N}$ ).

In figure 4a, the dependence of the stress at the centre of the contact region  $\sigma_0$  on the surface fraction  $\Phi$ , for an indentation of  $\zeta = 0.3 \mu\text{m}$  and the remaining parameter values given in table 1, is depicted. Going from right to left, when the surface fraction is  $\Phi = 1$ , the Hertzian value of  $\sigma_0$  is found. As  $\Phi$  decreases, the total load distribution over a smaller number of pillars induces a slightly larger apparent contact region, but it provokes a stress concentration, represented by an increase of  $\sigma_0$ , due to the reduction of the real contact area and the number of pillars in contact. If we continue to diminish  $\Phi$ , a monotonic growth of  $\sigma_0$  is observed until it saturates to a plateau. This saturation, which corresponds to an SFP behaviour, is completely attained when the surface fraction  $\Phi$  becomes small enough to leave just a single pillar within the contact region. In figure 4a, the Hertz-to-SFP transition is presented for different values of the ratio  $E_p/E_l$ , for the same indentation  $\zeta$ . A reduction of the system stiffness  $E_p/E_l$  enhances a decrease of the  $\sigma_0$

stress levels observed for both limits, Hertz and SFP. Despite this vertical shift, the general trend remains unchanged whatever the value of the ratio  $E_p/E_l$ .

In figure 4b, the real contact area  $\mathcal{A}$  is presented in terms of the apparent contact area  $\pi a^2$ , for a Young's moduli ratio  $E_p/E_l = 1$  and all other parameters given in table 1. The following description remains qualitatively valid for any value of the ratio  $E_p/E_l$ , presented in this work. Note that data corresponding to very small values of the surface fraction  $\Phi < 0.01$  are included but not visible, because they are superimposed near the origin since the real and apparent contact areas are equal and correspond to the top surface of a pillar  $\mathcal{A} = \pi a^2 = \pi d^2/4 \sim 5 \times 10^{-11} \text{ m}^2$ , which is two orders of magnitude smaller than most of the presented data. Describing each curve from right to left, when the indentation  $\zeta$  is small, both the apparent  $\pi a^2$  and the real  $\mathcal{A}$  contact areas are small, with  $\mathcal{A} < \pi a^2$ . As the applied total load  $F_T$ , the indentation  $\zeta$  and the apparent contact area  $\pi a^2$  are increased,  $\mathcal{A}$  grows monotonically and approaches the trend  $\Phi[\pi a^2]$ , for all the values of  $\Phi$ . For the highest values of the surface fraction  $\Phi$ , the real contact area  $\mathcal{A}$  approaches the Hertzian value  $\mathcal{A}_H$ , which is a circle of radius  $a = \sqrt{R\zeta}$ . As we diminish the surface fraction  $\Phi$ , the number of pillars in contact is reduced, provoking a drop of  $\mathcal{A}$ . At a certain value of  $\Phi$ , which is smaller for the highest Young's moduli ratios  $E_p/E_l$ , the real and apparent contact areas suddenly take the value of the SFP contact, i.e. the area of the top of a single pillar  $\mathcal{A}_S = \pi d^2/4$ .

## 5. Asymptotic cases

There are special situations for which the size of the contact region, the contact radius  $a$ , can be predicted analytically. They correspond to the two limiting cases of the surface fraction, which are depicted in figure 1:  $\Phi \rightarrow 1$  for Hertzian and  $\Phi \rightarrow 0$  for SFP contact. Both behaviours are briefly described in the following subsections.

### (a) Hertzian contact

Hertzian contact [1] occurs either when  $\Phi \rightarrow 1$  or when the contact radius is  $a \ll d/2$ . Under these conditions, the problem simplifies to an axisymmetric geometry for which the pillar array becomes a layer of finite thickness [40]. Considering infinite friction between the two bodies, the well-known stress field for Hertzian contact reads

$$\sigma(r) = \sigma_{0H} \sqrt{1 - \left(\frac{r}{a}\right)^2}, \quad (5.1)$$

where the contact radius is  $a = \sqrt{\zeta R}$ , and the stress magnitude  $\sigma_{0H}$ , perceived at the centre of the contact region  $r = 0$ , is computed from the total indentation  $\zeta$  as follows:

$$\sigma_{0H} = \frac{2}{\pi[\gamma_l + \gamma_s]} \sqrt{\frac{\zeta}{R}}. \quad (5.2)$$

Therefore, as the pillars/substrate had become a single entity,  $\sigma_{0H}$  is equally sensitive to a change in stiffness of any component of the system (lens and compound substrate). In addition, as it is explicitly indicated in equation (5.2), a larger value of the stress  $\sigma_{0H}$  is expected when an important indentation  $\zeta$  is imposed. It is also well known that the total force is  $F_T = (2\pi/3)R\zeta\sigma_{0H}$ .

### (b) Soft-flat-punch contact

When  $\Phi \rightarrow 0$ , a SFP elastic contact is observed, because only one pillar is in contact with the lens. In the case where  $E_p \gg E_l$ , we can consider that the pillars/substrate system is rigid  $\delta_0 = w_s(r, \theta) = 0$  and, if the top of the pillar is completely in contact with the lens  $a = d/2$ , the problem is described by a uniform normal displacement generated with a rigid flat punch [1,35,36]. The solution for the aforementioned problem corresponds to the superposition of the SFP solution, within a circular region at which uniform displacement is imposed. This situation, for which the well-known stress

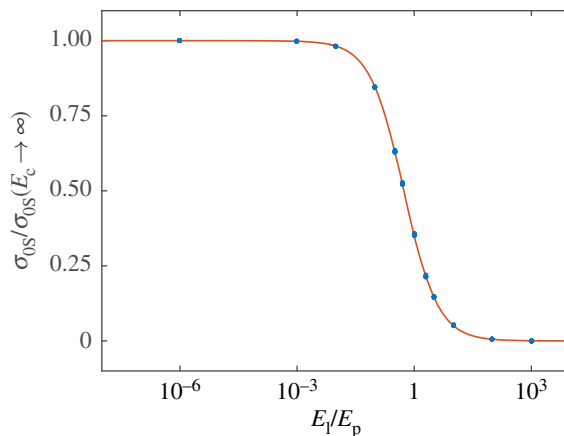


**Figure 5.** Stress at the centre of the pillar  $\sigma_{0S}$ , for the soft-flat-punch contact, as a function of the ratio of elastic moduli  $E_l/E_p$ , for  $\Phi = 2.3 \times 10^{-3}$  and the remaining values given in [table 1](#). The behaviour described by the continuous curve was computed with equation (5.8). (Online version in colour.)

field reads

$$\sigma(r) = \sigma_{0S}(E_p \rightarrow \infty) \left[ 1 - \left( \frac{2r}{d} \right)^2 \right]^{-1/2} \quad (5.3)$$

is valid for the lens–pillar–substrate system only for a total indentation  $\zeta$  that is smaller than the pillar height  $h$ . Herein, the stress magnitude  $\sigma_{0S}(E_p \rightarrow \infty)$  at  $r=0$ , the centre of the pillar, is computed from the total indentation  $\zeta$  as follows:

$$\sigma_{0S}(E_p \rightarrow \infty) = \frac{2\zeta}{\pi d \gamma_1}. \quad (5.4)$$

By contrast, the case for which  $E_p \simeq E_l$  does not presents an analytical model, and must be studied numerically [37]. Herein, we will name this case the ‘soft-flat-punch’ contact problem, for which we propose the following simple model. Considering that the total indentation  $\zeta$  equals the addition  $w_l(0, \theta) + w_s(0, \theta) + \delta_0$ , and the expressions  $F_0 = \pi d^2 \sigma_{0S}/2$  and  $w_{l,s}(0, \theta) = \pi d \gamma_{l,s} \sigma_{0S}/2$ , which come from the rigid-flat-punch solution (the latter by making  $\zeta = w_{l,s}(0, \theta)$  and  $\sigma_{0S}(E_p \rightarrow \infty) = \sigma_{0S}$  in equation (5.4)), and that the compression of the centre pillar is  $\delta_0 = 4hF_0/(\pi d^2 E_p)$ , we can write

$$\zeta \approx \frac{\pi d}{2} \left[ \gamma_l + \gamma_s + \frac{4h}{\pi d E_p} \right] \sigma_{0S}. \quad (5.5)$$

This relationship resembles a combination of springs in series, which configuration is described by an effective elastic parameter  $\gamma^*$  constructed as follows:

$$\gamma^* \approx \frac{1 - \nu_l^2}{E_l} \left\{ 1 + \left[ \frac{1 - \nu_s^2}{1 - \nu_l^2} \right] \frac{E_l}{E_s} + \frac{4hE_l}{\pi d [1 - \nu_l^2] E_p} \right\}. \quad (5.6)$$

In particular, when  $E_p \gg E_l$  and recalling that  $E_s = E_p$ , which corresponds to a rigid flat punch and an elastic half-space since the pillar/substrate can be taken as a rigid body, and also considering that  $\nu_l \sim \nu_p$  and  $h \sim d$ , leads us to recover  $\gamma^*(E_p \rightarrow \infty) = \gamma_l$ .

For the contact between the lens and a soft pillar, employing the effective elastic constant, we can define the stress at  $r=0$  as

$$\sigma_{0S} = \frac{2\zeta}{\pi d \gamma^*}. \quad (5.7)$$

In addition, for a constant total indentation  $\zeta$  and considering  $E_s = E_p$ , the comparison between the previous definition and equation (5.4) yields the following expression for  $\sigma_{0S}$  in terms of the

ratio of Elastic moduli  $E_l/E_p$ :

$$\sigma_{0S} = \sigma_{0S}(E_p \rightarrow \infty) \left\{ 1 + \left( \frac{1 - \nu_s^2}{1 - \nu_l^2} + \frac{4h}{\pi d[1 - \nu_l^2]} \right) \frac{E_l}{E_s} \right\}^{-1}. \quad (5.8)$$

In figure 5, this relationship is shown, where sigmoid behaviour shows an excellent agreement with the numerical results. For  $E_l/E_p < 10^{-3}$ , a saturation towards the Boussines–Cerruti solution is observed  $\sigma_{0S} \simeq \sigma_{0S}(E_p \rightarrow \infty)$ . As the ratio  $E_l/E_p$  increases, the value of  $\sigma_{0S}$  falls down, reaching a new plateau of level  $\sigma_{0S} \simeq 0$ , when  $E_l/E_p > 10^3$ . Therefore, in the latter regime, for which the lens is extremely soft compared with the pillar/substrate stiffness, the stress  $\sigma_{0S}$  is negligible.

## 6. Discussion

Starting with a relatively slight load, provoking the contact of the lens with a single pillar, the SFP contact behaviour is observed until a second pillar (six pillars at different angular position but the same radial coordinate) is touched by the lens, which is due to an increase of the load and, consequently, the total indentation. Under this circumstances, from the contact condition  $\Delta(r, \theta) = 0$ , we find the relationship between the indentation  $\zeta$  and the radial position  $r_S$ , at which a second pillar must be placed in order to be barely touched by the lens

$$R - \sqrt{R^2 - r_S^2} + \left[ \frac{2}{\Pi} \arcsin \left( \frac{d}{2r_S} \right) - 1 \right] \zeta = 0, \quad (6.1)$$

with  $\Pi = \pi + 4h/[d(\gamma_s + \gamma_l)E_s]$ . For a given  $\zeta$ , we can estimate the radial position  $r_S$  at which a second pillar may be reached and, consequently, the corresponding pitch distance  $e_S = r_S$  and the SFP threshold surface fraction

$$\Phi_S = \frac{\pi}{2\sqrt{3}} \left( \frac{d}{r_S} \right)^2. \quad (6.2)$$

Therefore, when the combination of both parameters, indentation  $\zeta$  and surface fraction  $\Phi$ , is such that  $\Phi < \Phi_S$ , only one pillar must be in contact with the lens.

Considering that  $R \gg r_S \gg d/2$ , for relatively large indentations  $\zeta \gg (3/2)^3 R(d/\Pi)^2$ , we can approximate the radial position with the expression  $r_S \approx \sqrt{2R\zeta}$ , which leads to a threshold surface fraction that scales as  $\Phi_S \sim d^2/(R\zeta)$ .

Now, from the opposite situation, we define  $\Phi_H$  as another threshold surface fraction, above which a Hertzian contact can be used to approximate the magnitude of the stress field at the centre of each pillar. For high values of  $\Phi$ , this behaviour has been discerned qualitatively from the numerical results, as it was shown in figure 3*b*. Nevertheless, for a given indentation and a set of elastic parameters, a quantitative estimation of  $\Phi_S$  is only achieved numerically.

Based on this insight, we introduce the reduced variables  $\sigma_0^*$ , the stress at the centre of the central pillar, and  $\Phi^*$ , the reduced surface fraction, defined as

$$\sigma_0^* = \frac{\sigma_0(\Phi) - \sigma_{0H}}{\sigma_{0S} - \sigma_{0H}} \quad \text{and} \quad \Phi^* = \frac{\Phi - \Phi_S}{\Phi_H}, \quad (6.3)$$

where  $\sigma_{0H}$  and  $\sigma_{0S}$  are the limiting stresses at  $r = 0$  for the Hertz and the SFP contact conditions, i.e. when  $\Phi < \Phi_H$  and  $\Phi > \Phi_S$ , respectively. Herein, both stress values  $\sigma_{0H}$  and  $\sigma_{0S}$  are obtained numerically for  $\Phi \sim 1$  and  $\Phi \sim 0$ , respectively, whereas  $\Phi_H$  and  $\Phi_S$  result from fitting the data of the curves shown in figure 4*a* and their equivalents for the different values of indentation  $\zeta$  and Young's modulus ratio  $E_p/E_l$  given in table 1.

As shown in figure 6*a*, all the data, including the curves in figure 4*a* and the results for different values of  $\zeta$ , collapse to a master curve when the reduced variables given in equation (6.3) are used. The following rational function,

$$\sigma_0^* = [1 + \Phi^*]^{-3}, \quad (6.4)$$

provides a good qualitative description of the general trend for  $\Phi^* \geq 1$ , and an excellent quantitative agreement for  $\Phi^* \in [0, 1 - \Phi_S/\Phi_H]$ . Therefore, the stress concentration and the

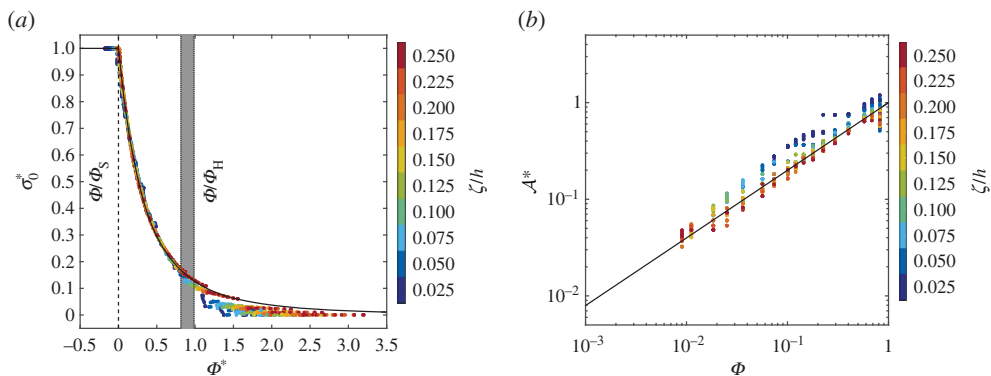


**Figure 6.** (a) Reduced stress at the centre of the pillar  $\sigma_0^*$  as function of the reduced surface fraction  $\Phi^*$  and (b) reduced real contact area  $\mathcal{A}^*$  as a function of the surface fraction  $\Phi$ , in the range  $0.05 \leq \zeta/h \leq 0.5 \mu\text{m}$  and for the parameters given in table 1. The trends depicted by the continuous lines [—], corresponds to the empiric relationships given by equation (6.4) for (a), and equation (6.6) for (b). (Online version in colour.)

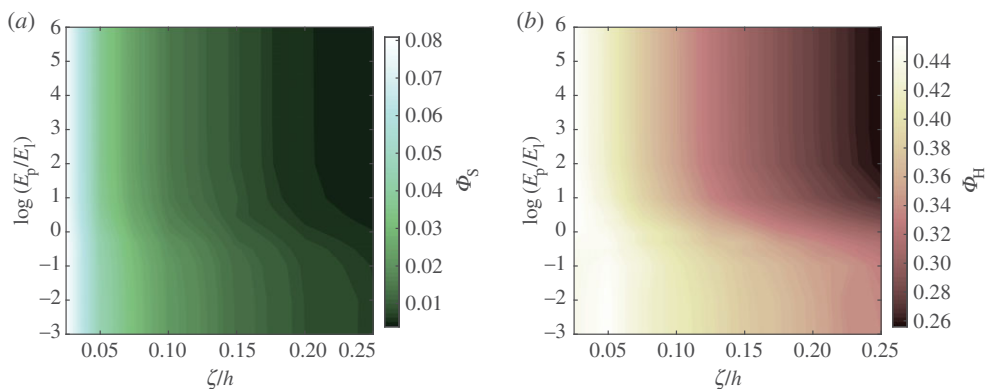


**Figure 7.** (a)  $\Phi_S$  and (b)  $\Phi_H$  as functions of the reduced indentation  $\zeta/h$ , in the range  $0.05 \leq \zeta/h \leq 0.5 \mu\text{m}$  and for the remaining parameters given in table 1. (Online version in colour.)

growth of  $\sigma_0$ , perceived during the transition from a Hertzian contact, along a discrete contact region, to a single punch-like contact, behaves as the inverse of the cube of a quantity that measures the separation from the limiting regimes: the difference of the surface fraction from the SFP threshold divided by the Hertz threshold value. Outside this transition zone, we recover the limiting cases: on one hand,  $\Phi^* = 0$  implies that  $\sigma_0^* = 1$  and, as a consequence, the SFP behaviour  $\sigma_0(\Phi) = \sigma_{0S}$  is expected, whereas on the other hand,  $\Phi^* = (1 - \Phi_S)/\Phi_H$  implies that  $\sigma_0^* \approx 0$  and a Hertzian contact  $\sigma_0(\Phi) \approx \sigma_{0H}$  should represent a good illustration of the discrete contact phenomenon.

The dependencies of  $\Phi_S$  and  $\Phi_H$  on the indentation  $\zeta$  and Young's modulus ratio  $E_p/E_l$  are depicted in figure 7a and b, respectively. For a fixed value of the ratio  $E_p/E_l$ , both threshold parameters  $\Phi_S$  and  $\Phi_H$  follow a similar monotonical decreasing tendency as the reduced indentation  $\zeta/h$  increases. The effect of the ratio  $E_p/E_l$  seems to be restricted to a shift towards larger values of both thresholds, strongly for  $\Phi_H$  and almost indistinguishably for  $\Phi_S$ . It is also important to note that the values that  $\Phi_S$  takes are an order of magnitude smaller than the values presented by  $\Phi_H$ .

For very small indentations  $\zeta/h < 0.025$ , the determination of the values of  $\Phi_S$  and  $\Phi_H$  becomes delicate, since the Hertzian and SFP stresses at  $r = 0$  present a very close magnitude  $\sigma_{0S} \sim \sigma_{0H}$ . Matching equations (5.2) and (5.7) gives the threshold indentation  $\zeta_T/h = [\gamma^*/(\gamma_l + \gamma_s)]^2 [d^2/Rh]$ ,

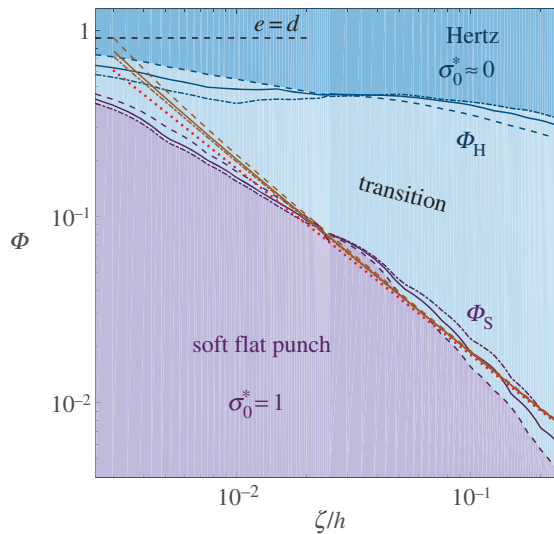


**Figure 8.** Phase diagram of the elastic contact regime. The phase space is given in terms of  $\Phi$  and the reduced indentation  $\zeta/h$ , for all the parameters given in table 1. The Hertz and soft-flat-punch (SFP) contact regions are bounded by the corresponding thresholds (violet and blue, respectively), which were obtained numerically. The thresholds are depicted with different line styles for the different values of Young's modulus ratio: dashed-dotted,  $E_p/E_l = 10^{-3}$ ; solid,  $E_p/E_l = 1$ ; dashed,  $E_p/E_l = 10^6$ . For the SFP threshold, the approximation given by equations (6.1) and (6.2) is shown as brown/straight curves for the three aforementioned Young's modulus ratio, whereas the large indentation approximation  $\Phi_S = \pi d^2 / (4\sqrt{3}R\zeta)$  corresponds to the overlapping red dotted straight lines. (Online version in colour.)

which for the parameters given in table 1 varies between  $0.004 \leq \zeta_T/h \leq 0.014$  and acts as an inferior boundary for the swept range of indentations. Nevertheless, an estimation of both parameters may be provided for  $\zeta/h < 0.025$ . From the curve of  $\sigma^*$  as a function of  $\Phi^*$  for the last performed fit, i.e. for  $\zeta/h = 0.025$ ,  $\Phi_H$  corresponds to the value of  $\Phi$  for which  $\sigma_0^* = 0.17$ , whereas  $\Phi_S$  is to the value of  $\Phi$  that makes  $\sigma_0^* = 0.92$ . Using this criterion,  $\Phi_H$  and  $\Phi_S$  can be approximated for  $\zeta/h < 0.025$ . This results are shown in figure 8 and will be discussed in the conclusion section.

We introduce the reduced variable  $\mathcal{A}^*$ , the dimensionless real contact area, defined as

$$\mathcal{A}^*(\Phi) = \frac{\mathcal{A}(\Phi) - \mathcal{A}_S}{\mathcal{A}_H - \mathcal{A}_S}, \quad (6.5)$$

where  $\mathcal{A}_H$  and  $\mathcal{A}_S$  are the limiting areas for the Hertz and the SFP contact conditions. Both values are obtained by computing the area of a circular region of radius  $a = \sqrt{R\zeta}$  for the Hertzian case, whereas  $a = d/2$  for the SFP situation. In figure 6b, all the data, including the curves in figure 4b and the results for different values of  $\zeta$ , show a similar behaviour when the reduced variable, given in equation (6.5), is used in combination with the surface fraction  $\Phi$ . The following power law

$$\mathcal{A}^* = \Phi^{0.7} \quad (6.6)$$

provides an accurate forecast for the general trend of the contact area in the range  $\Phi \in [10^{-2}, 10^0]$ . Note that only the contact area data for which  $\mathcal{A} < \mathcal{A}_S$  is visible in figure 4b, with logarithmic scales, since for an SFP contact situation  $\mathcal{A} = \mathcal{A}_S$  and the reduced area is  $\mathcal{A}^* = 0$ .

## 7. Conclusion

In the present work, the elastic contact between a spherical lens and a patterned substrate (hexagonal lattice of pillars) has been studied in depth, using a superposition method of discrete pressure elements. For relatively small indentations, a transition from a Hertzian elastic contact



behaviour towards a SFP contact, considering a uniform displacement of the pillars, was observed when the surface fraction of pillars on the substrate is increased. With the use of reduced variables for the stress at the centre of the central pillar and the surface fraction occupied by the pillars, all the results collapse into a master curve, for which a rational function describes the passage between the aforementioned limiting contact regimes. Additionally, a simple model to describe the behaviour of a soft-flat-punch contact between the lens and a single elastic pillar has been presented as a function of the pillar geometry and the elastic properties of the lens and the pillar-substrate. Special attention has been made on the effect of the ratio between Young's moduli of both bodies.

Finally, from the reduced surface traction, two threshold values are obtained: the Hertzian  $\Phi_H$  and the SFP  $\Phi_S$  limits. To summarize these results, a phase diagram is depicted in figure 8 in which axes correspond to the surface fraction  $\Phi$  and the reduced indentation  $\zeta/h$ . The SFP and Hertzian contact regions, which had been discerned from the numerical results, are shown. In brief, for a given indentation  $\zeta$ , if the surface fraction  $\Phi$  is greater than  $\Phi_H$ , the Hertzian contact offers a good approximation of the discrete contact phenomenon, whereas, if  $\Phi$  is smaller than  $\Phi_S$ , the system must have only one pillar in contact with the lens. In addition, also illustrated in figure 8, an analytical expression for the SFP threshold has been deduced from purely geometric considerations, which shows a good agreement with the numerical results, mainly in the large indentations regime. In this region, a simple theoretical approximation is also represented, for which the effect of the elastic parameters seems to be negligible. According to the theory developed by Greenwood and colleagues [5,6] based on a statistical approach, the dimensionless parameter  $\alpha = \mathcal{R}_a/\zeta$ , which is the ratio between the RMS roughness of the surfaces in contact  $\mathcal{R}_a$  and the total indentation  $\zeta$ , indicates the influence of the roughness on the contact mechanics. For the hexagonal array of cylinders, as the sphere is considered to be smooth,  $\mathcal{R}_a = h/2$ , yielding the expression for the Greenwood dimensionless parameter

$$\alpha = \frac{h}{2\zeta}. \quad (7.1)$$

Considering a threshold value of  $\alpha$ , which has been given the empirical value of  $\alpha = 0.05$  [6], below which the Hertz theory can be applied with confidence, a vertical line in the phase diagram shown in figure 8 at the value of  $\zeta/h = (2\alpha)^{-1}$  is found. Even though this assumption should be valid for large indentations  $\zeta/h \geq 10$ , also corresponding to large contact regions, this procedure wipes out completely the impact of the surface fraction  $\Phi$ , at the indentation regime presented here. Fortunately, a second dimensionless parameter  $\mu$  is also proposed by Greenwood and colleagues [5,6], required to forecast precisely the contact behaviour. For rough nominally flat surfaces,  $\mu$  depends only on the geometry, i.e. the roughness, the asperity density and the RMS curvature of the asperities, and only generates a secondary effect on the stress and displacement fields when the contact zone spans infinitely compared with the nominal size of the asperities. For the case presented herein, we expect that  $\mu$  will take the form  $\mu \sim \Phi \sqrt{\mathcal{R}\mathcal{R}_a}/d$ , which leads to an estimation of the second Greenwood dimensionless parameter:

$$\mu \sim \frac{\Phi}{d} \sqrt{\frac{\mathcal{R}h}{2}}, \quad (7.2)$$

where the effect of the surface fraction  $\Phi$  appears directly.

Thus, this analysis, which is a result of the qualitative comparison with Greenwood's theory, indicates that  $\Phi$  and  $\zeta/h$  are the correct dimensionless parameters required to describe the passage from Hertzian to SFP contact on periodically rough surfaces.

The methodology that we have developed allowed us to gain some insight on the discrete contact phenomenon. Nevertheless, it only represents some first steps and several important issues remain to be addressed. For instance, the case of large indentations, which are comparable in size with the height of the pillars  $\zeta \sim h$ , must be analysed separately. Under these circumstances, an intimate contact between the lens and the patterned surface, which has been studied with experiments [3,31,33,41], may be triggered, and the role of adhesion should be taken

into account. Our efforts are currently being focused on this problem, and the corresponding analysis will be presented in a future publication.

**Data accessibility.** The document supporting this article has been uploaded as part of the electronic supplementary material.

**Authors' contributions.** R.L.A. carried out the theoretical work, performed the numerical simulations, participated in the analysis of results and drafted the manuscript; E.R., L.L., F.R. and C.P. conceived of the study, participated in the analysis of results; F.R. and C.P. coordinated the study and helped draft the manuscript. All authors gave final approval for publication.

**Competing interests.** We declare we have no competing interests.

**Funding.** This project was carried out thanks to funding by the ANR (ANR-11-BS04-0030 project).

**Acknowledgements.** We wish to thank T. Salez for fruitful and very interesting discussions.

**Disclaimer.** The views and opinions expressed in this article are those of the authors.

## References

1. Johnson KL. 1985 *Contact mechanics*. Cambridge, UK: Cambridge University Press.
2. Restagno F, Crassous J, Cottin-Bizonne C, Charlaix E. 2002 Adhesion between weakly rough beads. *Phys. Rev. E*. **65**, 042301. (doi:10.1103/PhysRevE.65.042301)
3. Degrandi-Contraires E, Beaumont A, Restagno F, Weil R, Poulard C, Leger L. 2013 Cassie-Wenzel-like transition in patterned soft elastomer adhesive contacts. *Eur. Phys. Lett.* **101**, 14001. (doi:10.1209/0295-5075/101/14001)
4. Greenwood JA, Williamson JBP. 1966 Contact of nominally flat surfaces. *Proc. R. Soc. Lond. A* **295**, 300–319. (doi:10.1098/rspa.1966.0242)
5. Greenwood JA, Tripp JH. 1967 The elastic contact of rough spheres. *J. Appl. Mech.* **89**, 153–159. (doi:10.1115/1.3607616)
6. Greenwood JA, Johnson KL, Matsubara E. 1984 Surface roughness parameter in Hertz contact. *Wear* **100**, 47–57. (doi:10.1016/0043-1648(84)90005-X)
7. Li L, Etsion I, Talke FE. 2010 Elastic/plastic spherical contact modeling including roughness effects. *Tribol. Lett.* **40**, 357–363. (doi:10.1007/s11249-010-9716-z)
8. Beheshti A, Khonsari MM. 2014 On the contact of curved rough surfaces: contact behavior and predictive formulas. *J. Appl. Mech.* **81**, 1–15. (doi:10.1115/1.4028426)
9. Bush AW, Gibson RD, Thomas TR. 1975 The elastic contact of a rough surface. *Wear* **35**, 87–111. (doi:10.1016/0043-1648(75)90145-3)
10. Persson BNJ. 2006 Contact mechanics for randomly rough surfaces. *Surf. Sci. Rep.* **61**, 201–227. (doi:10.1016/j.surfrep.2006.04.001)
11. Johnson KL, Greenwood JA, Higginson JG. 1984 The contact of elastic regular wavy surfaces. *Int. J. Mech. Sci.* **27**, 383–396. (doi:10.1016/0020-7403(85)90029-3)
12. Block JM, Keer LM. 2008 Periodic contact problems in plane elasticity. *J. Mech. Mater. Struct.* **3**, 1207–1237. (doi:10.2140/jomms.2008.3.1207)
13. Archard JF. 1953 Contact and rubbing of flat surfaces. *J. Appl. Phys.* **24**, 1–8. (doi:10.1063/1.1721448)
14. Murarash B, Itovich Y, Varenberg M. 2011 Tuning elastomer friction by hexagonal surface patterning. *Soft Matter* **7**, 5553–5557. (doi:10.1039/c1sm00015b)
15. Brormann K, Barel I, Urbakh M, Bennewitz R. 2013 Friction on a microstructured elastomer surface. *Tribol. Lett.* **50**, 3–15. (doi:10.1007/s11249-012-0044-3)
16. Kligerman Y, Varenberg M. 2014 Elimination of stick-slip motion in sliding of split or rough surface. *Tribol. Lett.* **53**, 395–399. (doi:10.1007/s11249-013-0278-8)
17. Tsipenyuk A, Varenberg M. 2014 Use of biomimetic hexagonal surface texture in friction against lubricated skin. *J. R. Soc. Interface* **11**, 20140113. (doi:10.1098/rsif.2014.0113)
18. Romero V, Wandersman E, Debrégeas G, Prevost A. 2014 Probing locally the onset of slippage at a model multicontact interface. *Phys. Rev. Lett.* **112**, 1–5. (doi:10.1103/PhysRevLett.112.094301)
19. Mittal KL. 2004 Polymer surface modification: relevance to adhesion. In *Contact mechanics* (ed. KL Mittal), vol. 3. Boca Raton, FL: CRC Press.
20. Kozlova N, Santore MM. 2006 Manipulation of micrometer-scale adhesion by tuning nanometer-scale surface features. *Langmuir* **22**, 1135–1142. (doi:10.1021/la0515221)
21. Poulard C, Restagno F, Weil R, Leger L. 2011 Mechanical tuning of adhesion through micro-patterning of elastic surfaces. *Soft Matter* **101**, 2543–2551. (doi:10.1039/c0sm01099e)

22. Tamelier J, Chary S, Turner KL. 2012 Vertical anisotropic microfibers for a gecko-inspired adhesive. *Langmuir* **28**, 8746–8752. (doi:10.1021/la3004855)
23. Gorb S, Varenberg M, Peressadko A, Tuma J. 2007 Biomimetic mushroom-shaped fibrillar adhesive microstructure. *J. R. Soc. Interface* **4**, 271–275. (doi:10.1098/rsif.2006.0164)
24. Bhushan B, Jung YC. 2011 Natural and biomimetic artificial surfaces for superhydrophobicity, self-cleaning, low adhesion, and drag reduction. *Progress Mater. Sci.* **56**, 1–108. (doi:10.1016/j.pmatsci.2010.04.003)
25. Hui CY, Glassmaker N, Tang T, Jagota A. 2004 Design of biomimetic fibrillar interfaces: 2. Mechanics of enhanced adhesion. *J. R. Soc. Interface* **1**, 35–48. (doi:10.1098/rsif.2004.0005)
26. Zhou M, Pesika N, Zeng H, Tian Y, Israelachvili J. 2013 Recent advances in gecko adhesion and friction mechanisms and development of gecko-inspired dry adhesive surfaces. *Friction* **1**, 114–129. (doi:10.1007/s40544-013-0011-5)
27. Crosby AJ, Hageman M, Duncan A. 2005 Controlling polymer adhesion with ‘pancakes’. *Langmuir* **21**, 11 738–11 743. (doi:10.1021/la051721k)
28. Murphy MP, Kim S, Sitti M. 2009 Enhanced adhesion by gecko-inspired hierarchical fibrillar adhesives. *ACS Appl. Mater. Interfaces* **1**, 849–855. (doi:10.1021/am8002439)
29. Benz M, Rosenberg KJ, Kramer EJ, Israelachvili JN. 2006 The deformation and adhesion of randomly rough and patterned surfaces. *J. Phys. Chem. B* **110**, 11 884–11 893. (doi:10.1021/jp0602880)
30. Greiner C, del Campo A, Arzt E. 2007 Adhesion of bioinspired micropatterned surfaces: effects of pillar radius, aspect ratio, and preload. *Langmuir* **23**, 3495–3502. (doi:10.1021/la0633987)
31. Verneuil E, Ladoux B, Buguin A, Silberzan P. 2007 Adhesion on microstructured surfaces. *J. Adhesion* **83**, 449–472. (doi:10.1080/00218460701377529)
32. Hisler V, Palmieri M, Le Houerou V, Gauthier C, Nardin M, Vallat MF, Vonna L. 2013 Scale invariance of the contact mechanics of micropatterned elastic substrates. *Int. J. Adhesion Adhesiv.* **45**, 144–149. (doi:10.1016/j.ijadhadh.2013.04.006)
33. Nadermann N, Ning J, Jagota A, Hui CY. 2010 Active switching of adhesion in a film-terminated fibrillar structure. *Langmuir* **26**, 15 464–15 471. (doi:10.1021/la102593h)
34. Love AEH. 1952 *A treatise on the mathematical theory of elasticity*, 4th edn. Cambridge, UK: Cambridge University Press.
35. Harding JW, Sneddon IN. 1945 The elastic stresses produced by the indentation of the plane surface of a semi-infinite elastic solid by a rigid punch. *Math Proc Cambridge* **41**, 16–26. (doi:10.1017/S0305004100022325)
36. Maugis D. 2000 *Contact, adhesion and rupture of elastic solids*. Berlin, Germany: Springer.
37. Gecit MR. 1986 Axisymmetric contact problem for a semi-infinite cylinder and a half-space. *Int. J. Eng. Sci.* **24**, 1245–1256. (doi:10.1016/0020-7225(86)90054-6)
38. Guidoni GM, Schillo D, Hangen U, Castellanos G, Arzt E, McMeeking RM, Bennewitz R. 2010 Discrete contact mechanics of a fibrillar surface with backing layer interactions. *J. Mech. Phys. Solids* **58**, 1571–1581. (doi:10.1016/j.jmps.2010.07.009)
39. Noderer WL, Shen L, Vajpayee S, Glassmaker NJ, Jagota A, Hui CY. 2007 Enhanced adhesion and compliance of film-terminated fibrillar surfaces. *Proc. R. Soc. A* **463**, 2631–2654. (doi:10.1098/rspa.2007.1891)
40. Li J, Chou TW. 1997 Elastic field of a thin-film/substrate system under an axisymmetric loading. *Int. J. Solids Struct.* **34**, 4463–4478. (doi:10.1016/S0020-7683(97)00053-X)
41. Dies L, Restagno F, Weil R, Leger L, Poulard C. 2015 Role of adhesion between asperities in the formation of elastic solid/solid contacts. *Eur. Phys. J. E* **38**, 1–8. (doi:10.1140/epje/i2015-15130-4)